



Cite this: *Nanoscale*, 2023, **15**, 19735

Electrical and optoelectronic anisotropy and surface electron accumulation in ReS₂ nanostructures†

Hemant Kumar Bangolla,^a Muhammad Yusuf Fakhri,^a Ching-Hsuan Lin,^a Cheng-Maw Cheng,^{b,c,d,e} Yi-Hung Lu,^f Tsu-Yi Fu,^f Pushpa Selvarasu,^a Rajesh Kumar Ulaganathan,^g Raman Sankar^g and Rwei-San Chen^{h*}

Two interesting electronic transport properties including in-plane anisotropy and nonhomogeneous carrier distribution were observed in ReS₂ nanoflakes. The electrical conductivity defined by the current parallel to the *b*-axis ($\parallel b$) is 32 times higher than that perpendicular to the *b*-axis ($\perp b$). Similar anisotropy was also observed in optoelectronic properties in which the ratio of responsivity $\parallel b$ to $\perp b$ reaches 20. In addition, conductivity and thermal activation energy with substantial thickness dependence were observed, which indicates a surface-dominant 2D transport in ReS₂ nanoflakes. The presence of surface electron accumulation (SEA) in ReS₂ has been confirmed by angle-resolved photoemission spectroscopy and scanning tunneling spectroscopy. The electron concentration ($\sim 10^{19}$ cm⁻³) at the surface is over three orders of magnitude higher than that of the bulks. Sulfur vacancies which are sensitive to air molecules are suggested to be the major factor resulting in SEA and high conductivity in ReS₂ nanostructures.

Received 24th September 2023,

Accepted 15th November 2023

DOI: 10.1039/d3nr04830f

rsc.li/nanoscale

1. Introduction

Transition metal dichalcogenides (TMDs) are a group of two-dimensional (2D) layered semiconductors that share a typical sandwich structure in the form of MX₂, where M is a transition metal (such as Mo, Re, Ti or W) and X is a chalcogen atom (such as S, Se or Te).^{1,2} The remarkable mechanical and optoelectronic properties of TMDs make them thought-provoking for potential use in applications such as high-end electronics, flexible electronics, optoelectronics, spintronics, and energy harvesting.^{3,4} Recently, rhenium disulfide (ReS₂) has gained researchers' great attention due to its distinct properties such as weak inter-layer coupling, electrical, and optical anisotropic properties.^{5–8} Moreover, ReS₂ crystallizes in a distorted one-trigonal (1T) phase with lower plane symmetry^{9,10} unlike most

explored TMDs such as MoS₂ and WS₂ with a 2H phase.^{11,12} A strong electronic and vibrational decoupling produced by this exceptional crystal structure of ReS₂ generates some exceptional physical and chemical properties. ReS₂ possesses a direct band gap from the monolayer (1.43 eV) to the bulk (1.35 eV),^{13–15} which is superior to other TMDs with an indirect bandgap in their bulk form.^{16,17} This thickness-independent direct band gap property makes ReS₂ an ideal candidate for fabricating novel optoelectronic devices irrespective of the thickness.

Anisotropy is an interesting phenomenon, in which the non-symmetry in structure induces angle-dependent properties that facilitate the modulation of properties with an extra degree of freedom. ReS₂ is one of the prominent materials in which the quasi 1D Re₄ chains (*b*-axis) develop distinct anisotropic properties.^{18,19} In ReS₂, the two anisotropic axes are corresponding to the crystal directions with the shortest (*b*-axis) and second-shortest (*a*-axis) axes with an angle difference of $\sim 60^\circ$ or $\sim 120^\circ$.^{10,14} The unique crystal structure of ReS₂ along with its strong in-plane anisotropy leads to its extensive utilization in the development of functional devices including field effect transistors (FETs), polarized pulse generators, polarization-sensitive photodetectors, digital inverters, and energy storage and electrocatalysis devices.^{14,20–23} Liu *et al.* demonstrated an integrated digital inverter by the fabrication of two FETs on the same ReS₂ flake.¹⁴ Liu *et al.* reported a polarization-sensitive photo-

^aGraduate Institute of Applied Science and Technology, National Taiwan University of Science and Technology, Taipei 10607, Taiwan. E-mail: rsc@mail.ntust.edu.tw

^bNational Synchrotron Radiation Research Center, Hsinchu 30076, Taiwan

^cDepartment of Physics, National Sun Yat-sen University, Kaohsiung 80424, Taiwan

^dDepartment of Electrophysics, National Yang Ming Chiao Tung University, Hsinchu 300, Taiwan

^eTaiwan Consortium of Emergent Crystalline Materials, National Science and Technology Council, Taipei 10601, Taiwan

^fDepartment of Physics, National Taiwan Normal University, Taipei 11677, Taiwan

^gInstitute of Physics, Academia Sinica, Taipei 115201, Taiwan

†Electronic supplementary information (ESI) available. See DOI: <https://doi.org/10.1039/d3nr04830f>

10.1039/d3nr04830f

detector using the anisotropic structure of ReS₂ and investigated the effect of the polarization angle of incident light on the photocurrent.²¹ These findings gave rise to a novel technique for designing optoelectronic devices that makes use of the lattice anisotropy. In addition to this, TMDs can be exploited to develop practical integrated optical applications by utilizing the unique properties of low symmetry.²³

In general, for a majority of n-type semiconductors, an electron depletion layer was observed at their surfaces due to the Fermi level pinned within the band gap. However, some n-type semiconductors such as InN,^{24,25} InAs,²⁶ InGaN,²⁷ SnO₂,²⁸ and In₂O₃^{29,30} show an electron accumulation layer at the surface due to the Fermi level pinned above the conduction band minimum (CBM). Recently, a high electron concentration at MoS₂³¹ and MoSe₂³² surfaces has been observed due to surface electron accumulation (SEA). In-layered TMD materials which are dangling-bond-free have less surface states, hence the SEA in TMDs is somewhat unexpected. The SEA can play a significant role in novel devices such as photodetectors, gas sensors, FETs, and catalysis devices.^{32–37} The availability of more surface electrons can greatly influence the efficiency of these devices. Therefore, understanding the origin and nature of SEA is challenging and of great importance in the design and analysis of high-performance TMD-based device applications.

In this work, we have investigated anisotropy in electrical and optoelectronic properties along with SEA in ReS₂ nanoflakes. The dark conductivity and photoconductivity with charge transport parallel and perpendicular to the crystallographic *b*-axis were measured and their ratios were estimated. In addition, thickness-dependent conductivity and activation energy were observed, suggesting a surface-dominant electronic transport. The unique surface characteristic with a high electron concentration in ReS₂ single crystals has also been confirmed and discussed.

2. Results and discussion

2.1. Structural characterization of ReS₂ bulk crystals

Fig. 1a shows a photograph of a ReS₂ single crystal with a length of 6 mm. The XRD pattern of an aligned ReS₂ single crystal is shown in Fig. 1b. The existing diffraction peaks at

14.6, 29.4, 44.7, and 60.9° are consistent with the (001), (002), (003), and (004) planes of the triclinic 1T structure of ReS₂ (JCPDS #520818).^{38,39} The Raman spectrum of ReS₂ crystals is presented in Fig. 1c. The observed series of Raman modes are also consistent with the triclinic 1T structure of ReS₂.^{13,40} The most intense peaks identified at 149.5 and 210.1 cm⁻¹ with a full width at half maximum (FWHM) of 2.96 and 3.16 cm⁻¹ respectively are typically first-order E_{2g} (in-plane) and A_g-like (out-of-plane) vibrational modes respectively.²¹ The narrow peak broadening is an indication of high-quality single-crystalline ReS₂ grown by the CVT method. The identified Raman modes in the range of 100–310 cm⁻¹ are attributed to symmetry splitting in the 1T structure of ReS₂. The second-order Raman modes were also observed in the region of 310–450 cm⁻¹.⁴¹

2.2. Electrical and optoelectronic anisotropy in ReS₂ nanoflakes

2.2.1. Dark conductivity anisotropy. To investigate the anisotropy of electronic transport, crystal orientations of individual ReS₂ nanoflakes were identified by polarized Raman spectroscopy prior to electrode fabrication. Actually, the crystallographic *b*-axis of stripped flakes is possible to be recognized by their geometry. We noticed that ReS₂ crystals are easier to be cracked along the *b*-axis with Re chains. This property makes the exfoliated nanoflakes rectangle- or stripe-like and the longer side is mostly parallel to the *b*-axis. Fig. 2a and b show the AFM images and height profiles of the ReS₂ nanoflake devices with the electrodes fabricated parallel and perpendicular to the *b*-axis respectively.

The crystal orientations of the selected nanoflakes for device fabrication were verified by Raman measurement. According to the literature, the relative intensity of the A_g-like peak (210 cm⁻¹) to E_g (150 cm⁻¹) reaches the maximal/minimal when laser polarization is parallel (*E*||*b*)/perpendicular (*E*⊥*b*) to the *b*-axis. Fig. 2c depicts the Raman spectra of a typical ReS₂ nanoflake strip measured at *E*||*b* and *E*⊥*b*. The enhanced peaks at 210 cm⁻¹ (A_g-like) and 150 cm⁻¹ (E_g) for the polarization at *E*||*b* and *E*⊥*b* respectively are consistent with the previous reports.^{21,42} Based on this approach, the long edge of the nanoflakes parallel (Fig. 2a) and perpendicular (Fig. 2b) to the *b*-axis was examined and confirmed by the polarized Raman measurements.

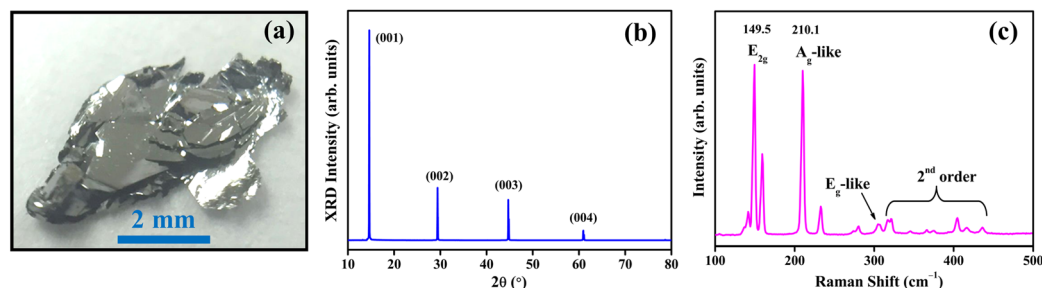


Fig. 1 (a) Photograph, (b) XRD pattern, and (c) Raman spectrum of a CVT-grown ReS₂ bulk crystal.

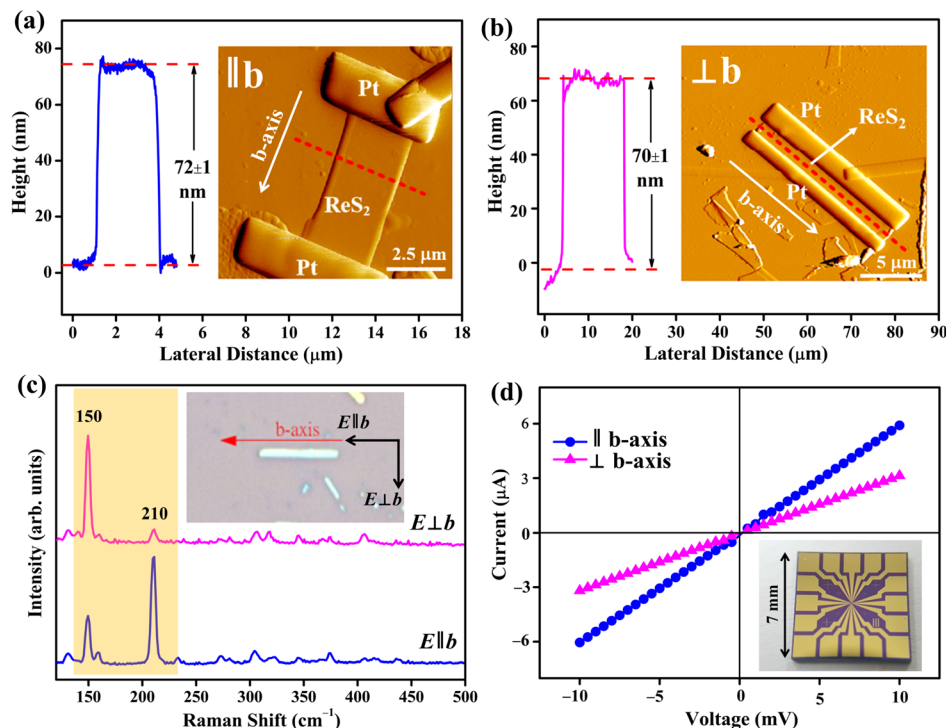


Fig. 2 AFM height profiles and images of (a) a nanoflake $\parallel b$ and (b) a nanoflake $\perp b$. (c) Polarization-dependent Raman spectra of the ReS_2 nanoflakes. (d) I - V curves of ReS_2 nanoflakes $\parallel b$ and $\perp b$. The inset shows the SiO_2 (300 nm)/ n^+ -Si chip template used for the FIB fabrication of ReS_2 nanoflake devices.

Fig. 2d shows the I - V measurements of the ReS_2 nanoflakes measured along different crystal orientations ($\parallel b$ and $\perp b$). The linear nature of the curves indicates the good ohmic contact between ReS_2 nanoflakes and FIB-fabricated Pt electrodes. To eliminate the thickness effect on the conductivity, the thickness of nanoflakes $\parallel b$ (72 nm) and $\perp b$ (70 nm) was maintained almost similar. The conductance with current flow parallel and perpendicular to the b -axis is respectively denoted as $G_{\parallel b}$ and $G_{\perp b}$ and is obtained from the slope of the I - V curves. The conductivity (σ) values were calculated from the following equation:⁴³

$$G = \frac{I}{V} = \sigma \frac{wt}{l}, \quad \sigma = G \frac{l}{wt}, \quad (1)$$

where w , t , and l are the width, thickness, and length of the conducting channel respectively. The calculated conductivities of nanoflakes $\parallel b$ ($\sigma_{\parallel b}$) and $\perp b$ ($\sigma_{\perp b}$) are 160 and 5 $\Omega^{-1} \text{cm}^{-1}$ respectively. From this result, it is clear that $\sigma_{\parallel b}$ is much higher than $\sigma_{\perp b}$ ($\sigma_{\parallel b}/\sigma_{\perp b} = 32$). Theoretically, the conductivity is independent of sample dimensions and only depends on two intrinsic quantities including the carrier concentration (n) and mobility (μ), i.e. $\sigma = en\mu$, where e is the elementary charge. The higher $\sigma_{\parallel b}$ is consistent with the result in ReS_2 bulks ($\sigma_{\parallel b}/\sigma_{\perp b} \sim 10$), which is attributed to the higher mobility due to the presence of the strongest bonding force along the crystal orientation of the Re-chains.⁴⁴ The orientation-dependent electron concentration can be excluded though the conductivity also depends on the carrier concentration. The temperature-depen-

dent conductivity measurements show both $\sigma_{\parallel b}$ and $\sigma_{\perp b}$ with almost the same activation energy of the carrier, which indicates the same donor type and carrier concentration (see Fig. S1 and Note S1, ESI†).

2.2.2. Photoconductivity anisotropy. To investigate the anisotropy in optoelectronic properties of ReS_2 nanoflakes, photoconductivity studies were performed for different orientation nanoflakes. The photoresponse measurements of ReS_2 nanoflake $\parallel b$ and $\perp b$ devices were carried out at a bias of 0.1 V under an excitation wavelength of 532 nm, as illustrated in Fig. 3a. To obtain the photocurrent values, the dark current values were subtracted from the response curves. The photocurrent of both nanoflake devices increases with the increase of light power. The nanoflake $\parallel b$ shows higher photoresponse than the nanoflake $\perp b$. The photocurrent (i_p) vs. light intensity (I) plots of the nanoflakes $\parallel b$ and $\perp b$ are depicted in Fig. 3b. The photocurrent of the nanoflake $\parallel b$ device is approximately three times higher than that of the nanoflake $\perp b$ device. Both devices exhibit a linear relationship of the photocurrent and light intensity, suggesting that the ReS_2 nanostructures can be a suitable photodetector material for operation in the linear region.

Photodetector performance can be evaluated by the responsivity (R) which is defined as the ratio of the generated photocurrent (i_p) to the incident light intensity (I) on the active area (A) of a device ($R = i_p/IA$).^{45,46} The R values of ReS_2 nanoflake $\parallel b$ and $\perp b$ devices were calculated for different light intensities and are represented in Fig. 3c. An intensity-independent be-

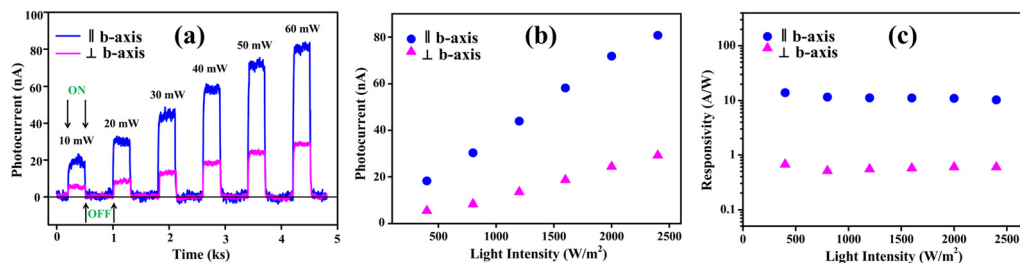


Fig. 3 Optoelectronic anisotropy in ReS₂ nanoflakes. (a) Photocurrent response measurements of ReS₂ nanoflake ||*b* and ⊥*b* devices under escalating illumination powers at a wavelength of 532 nm and a bias of 0.1 V. The ON and OFF show the illuminating source conditions. (b) The photocurrent versus light intensity and (c) the responsivity versus light intensity of the nanoflakes ||*b* and ⊥*b*.

havior of responsivity of both devices was observed. The average *R* values for the nanoflake ||*b* (*R*_{||*b*}) and ⊥*b* (*R*_{⊥*b*}) devices are 11.5 ± 1.25 and 0.58 ± 0.05 A W⁻¹ respectively. The nanoflake ||*b* shows better performance compared to the nanoflake ⊥*b* and *R*_{||*b*} is much higher than *R*_{⊥*b*} (*R*_{||*b*}/*R*_{⊥*b*} = 20). The optimal *R* value of our nanoflake device ≈ 14 A W⁻¹ is higher than the reported value (4 A W⁻¹) for ReS₂ multilayer photodetectors.¹ The higher *R* could also be explained by the higher mobility in the nanoflake ||*b* because *R* is linearly dependent on the mobility.^{47,48}

2.3. Dimension-dependent electronic transport properties

2.3.1. Thickness-dependent conductivity. The transport property studies were all based on the nanoflakes ||*b* in the later sections due to the devices of ReS₂ nanoflakes ||*b* with longer length and are easier for FIB electrode fabrication. Fig. 4a and b depict the conductance and its corresponding conductivity of ReS₂ nanoflakes and bulks with various thicknesses in the range of 23–222 nm and 10–100 μm respectively. Theoretically, the conductivity is an intrinsic property and is independent of the thickness according to eqn (1). However, the conductivity of nanoflakes shows substantial thickness dependence, and follows an inverse power law of $\sigma \propto t^{-\beta}$, where $\beta = 1.1$. The conductivity value increases from 12 to 430 Ω⁻¹ cm⁻¹, with the thickness decreasing from 222 to 23 nm. The values of nanoflakes are also nearly three to four orders of magnitude higher than the bulk values (0.012–0.038 Ω⁻¹ cm⁻¹). In principle, the nanoflakes were stripped from the bulk crystals and should have the same defect (doping) concentration or conductivity. The increasing conductivity due to thickness decrease implies that the majority carriers were dominated by the surface rather than the inner bulk.

2.3.2. Thickness-dependent activation energy. A similar phenomenon of thickness dependence was also observed in the temperature (*T*)-dependent conductivity of a ReS₂ nanoflake ||*b* (*t* = 90 nm) and a bulk (*t* = 10 μm), as shown in Fig. 4c. The σ vs. *T* curves were normalized by the σ at 300 K. The conductivity decrease with the decrease in temperature from 300 to 170 K shows the thermal activation behavior of semiconductors. In addition, we noticed that the conductivity of the nanoflake is less sensitive to the temperature compared with the bulk. The thermal activation energy (*E*_a) of the

majority carriers was calculated from the slope of the Arrhenius plot ($\ln\sigma$ vs. $1000/T$ graph) using the equation:⁴⁹

$$\sigma(T) = \sigma_0 \exp(-E_a/kT), \quad (2)$$

where *k* is the Boltzmann constant and σ_0 is the conductivity at *T* = 0 K. The curve fitting indicates the nanoflake with the activation energy at 5 meV, which is much lower than the value (170 meV) of the bulk, Fig. 4d. The distinct activation energy means different defect (donor) origins of the majority carriers. This observation also implies that the majority electrons come from the surface, which is consistent with the thickness-dependent conductivity result.

2.3.3. Transfer length method (TLM). According to the conventional 3D TLM model, the total resistance (*R*_T) between two metal electrodes is given by:^{31,50}

$$R_T = 2R_C + R_S = 2R_C + \rho_{3D} \frac{l}{wt}, \quad (3)$$

where *R*_C and *R*_S are the contact resistance and semiconductor resistance respectively and ρ_{3D} is the resistivity of the 3D conductor. Generally, *R*_T is linearly dependent on *l/wt*. The values of *R*_C and ρ_{3D} can be obtained from the linear fitting of the *R*_T vs. *l/wt* plot, as illustrated in Fig. 4e. It is clear that *R*_T data points were scattered and do not follow a clear linear relationship with *l/wt*. However, the *R*_T vs. *l/w* curve shows better linearity when a 2D conductor is assumed. In a 2D conductor, the resistance *R*_S is independent of the conductor thickness and only depends on the length and width of the conductor. Hence, the 2D TLM model can be given as:³¹

$$R_T = 2R_C + R_S = 2R_C + \rho_{2D} \frac{l}{w}, \quad (4)$$

where ρ_{2D} is the resistivity of the 2D conductor or sheet resistance.⁵¹ The 2D TLM plot is depicted in Fig. 4f. By linear fitting, the obtained *R*_C and ρ_{2D} are 400 ± 350 Ω and 1200 ± 160 Ω respectively. The TLM analysis reveals that ReS₂ nanoflakes follow a 2D transport behavior instead of a conventional 3D transport. This result further supports the probable surface-dominant conduction in ReS₂.

In addition, the specific contact resistance (*R*_{SC}) of ReS₂ nanoflakes with Pt electrodes is given by $R_{SC} = R_C w$,³¹ where *w* is the width of ReS₂ nanoflake devices which is typically in the

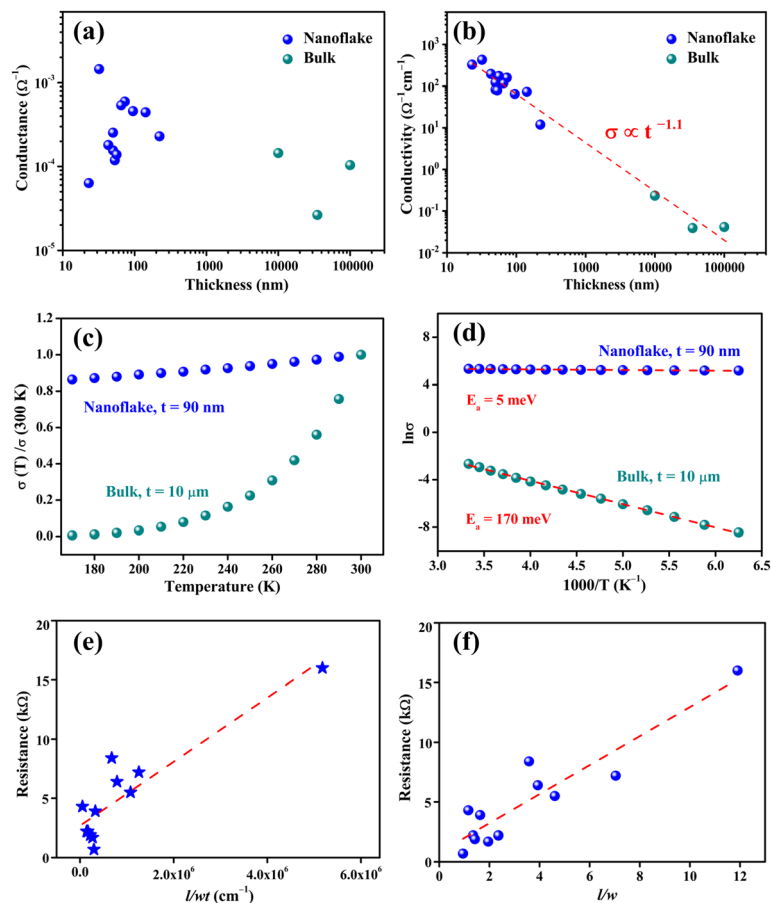


Fig. 4 Dimension-dependent electronic transport properties in ReS₂. (a) The electrical conductance and (b) the electrical conductivity of ReS₂ nanoflake and bulk with different thicknesses. (c) Curves of temperature-dependent conductivity $\sigma(T)$ and (d) their corresponding Arrhenius plots for a ReS₂ nanoflake ($t = 90$ nm) and a bulk crystal ($t = 10$ μm). The $\sigma(T)$ values in (c) were normalized by their corresponding conductivity values at 300 K, $\sigma(300$ K), to reveal the different temperature dependence of σ between the nanoflake and the bulk. (e) 3D TLM (resistance vs. l/wt) plot and (f) 2D TLM (resistance vs. l/w) plot of ReS₂ nanoflake devices. The red dash lines show the fitting of the experimental data points.

range of 0.6–9 μm . The calculated values of R_{SC} for the ReS₂–Pt interface are in the range of 0.24–3.6 $\text{k}\Omega \mu\text{m}$. These values are lower than the reported values for the ReS₂–Cr interface (5–175 $\text{k}\Omega \mu\text{m}$)⁵² which concludes that FIB fabricated Pt electrodes provide low contact resistance. The low contact resistance could be due to the formation of a conducting amorphous alloy layer between Pt and ReS₂.³¹ At the ReS₂–Pt interface, the alloy buffer layer can reduce native oxides, surface contaminants, the Schottky effect, and thus the contact resistance. The low contact resistance produced by FIB has also been observed in our previous studies in MoS₂ and MoSe₂.^{31,32}

2.4. SEA evidenced by angle-resolved photoemission spectroscopy (ARPES)

ARPES measurements were performed to get direct evidence of the surface-controlled transport in ReS₂. The valence bands of the *in situ*-cleaved (fresh), short aging (20 min exposure in air), and long aging (11 days exposure in air) surfaces are illustrated in Fig. 5a–c respectively. Here, the *in situ*-cleaved surface indicates the fresh surface cleaved in an ultra-high vacuum ($<1.8 \times$

10^{-10} Torr). The band mapping result shows a clear shift in valence band maxima (VBM) relative to the Fermi level for different surface conditions of ReS₂. The normal emission spectra at the Γ point of different ReS₂ surfaces are depicted in Fig. 5d and e. All samples show a sharp valence band edge, which is an indication of the high crystallinity of the CVT-grown ReS₂ single crystals. For the *in situ*-cleaved surface, the energy difference between the Fermi level (E_{F}) and VBM (E_{V}) is 1.22 eV, which indicates that the Fermi level is 0.13 eV below the conduction band minimum (CBM) (E_{C}), considering that the bandgap of bulk ReS₂ is around 1.35 eV.¹³ The electron carrier concentration (n) can be calculated from the following equation:⁵³

$$n = N_{\text{C}} \exp \left[\frac{-(E_{\text{C}} - E_{\text{F}})}{kT} \right], \quad (5)$$

where N_{C} is the effective density of states function in the conduction band. The calculated N_{C} is 8.35×10^{18} – 1.79×10^{19} cm^{-3} from $N_{\text{C}} = 2(2m_{\text{e}}^*kT/h^2)^{3/2}$. Here, m_{e}^* is the effective mass of an electron, and h is Planck's constant. The m_{e}^* is in the range of 0.48–0.8 m_0 for bulk ReS₂, where m_0 is the free

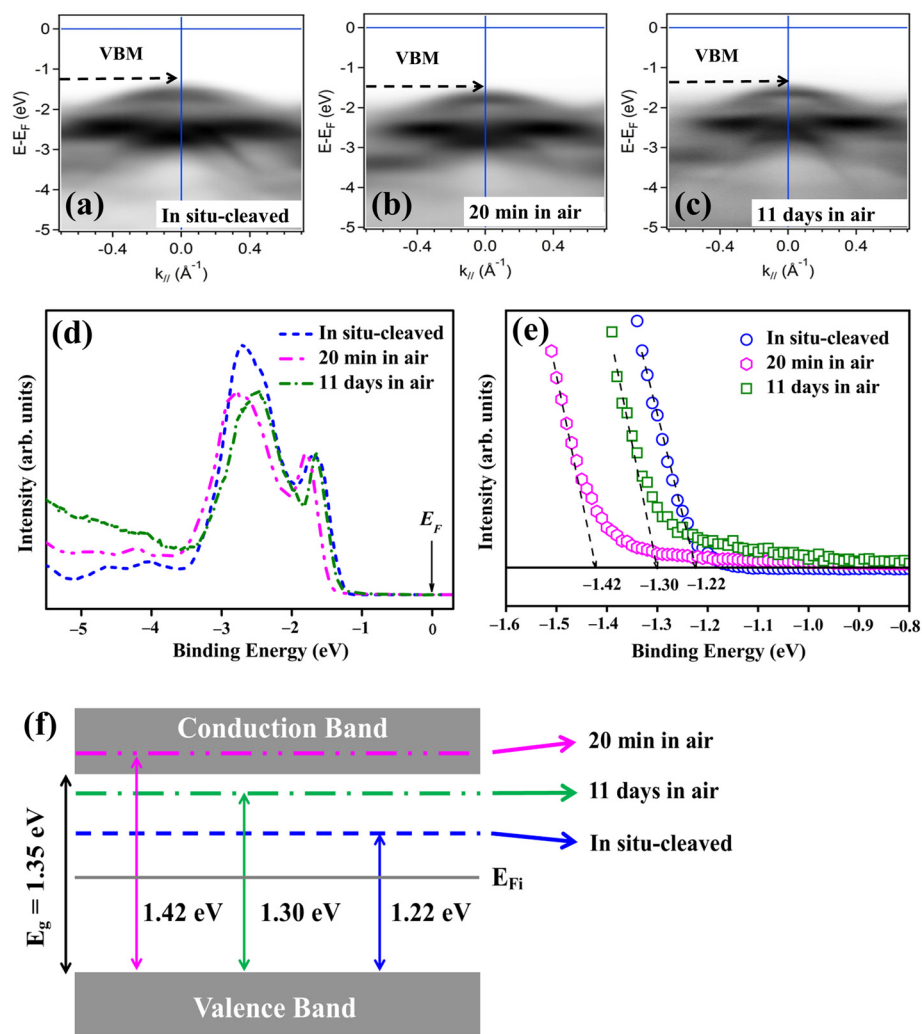


Fig. 5 ARPES characterization of different surfaces of ReS₂ single crystal. *E* vs. *k*_∥ valence band structures of the (a) *in situ*-cleaved, (b) short aging (20 min in air), and (c) long aging (11 days in air) surfaces of ReS₂ single crystals. (d) Normal emission spectra and (e) magnified normal emission spectra at the Γ point for the *in situ*-cleaved and aging surfaces of ReS₂ single crystals. (f) Schematic of the Fermi level shift for the different surface conditions.

electron rest mass.^{54,55} The calculated n at 5.5×10^{16} – 1.2×10^{17} cm⁻³ for the *in situ*-cleaved surface is lower than the values (1×10^{18} – 8.6×10^{18} cm⁻³) of ReS₂ nanoflakes^{56,57} and is relatively close to the value ($\sim 5.5 \times 10^{15}$ cm⁻³) of ReS₂ bulks in the previous reports,⁵⁸ which indicates that the fresh surface could have a quality similar to the bulk interior.

It should be noted that a clear energy shift of VBM from -1.22 to -1.42 eV was observed for the short aging surface, as shown in Fig. 5e. The corresponding Fermi level shift to beyond CBM ($E_F - E_C = 0.07$ eV) shows the n-type degenerate semiconductor character and its n value is given by:^{32,48}

$$E_F - E_C = kT \left[\ln \left(\frac{n}{N_C} \right) + 2^{-3/2} \left(\frac{n}{N_C} \right) \right]. \quad (6)$$

The calculated n increases to the level of 3.2×10^{19} – 6.9×10^{19} cm⁻³. The remarkable increase of the electron concen-

tration for over two orders of magnitude compared to the *in situ*-cleaved surface confirms that high-density electrons in the intrinsic (fresh) surface can be easily generated by simple exposure to air for 20 min. This observation also confirms the presence of SEA in ReS₂. In addition, it is interesting to note that a longer exposure (11 days) in air did not further increase but instead decrease the electron concentration. Fig. 5e shows that the VBM shifts back to -1.30 eV ($E_C - E_F = 0.05$ eV) and the electron concentration drops to 1.2×10^{18} – 2.6×10^{18} cm⁻³ for the long-term aging surface.

According to the previous reports, sulfur and selenium vacancies are the major causes of SEA in TMDs like MoS₂ and MoSe₂.^{31,32} In ReS₂, among various point defects, sulfur vacancies have the lowest formation energy (1.16–2.03 eV).⁵⁹ The sulfur vacancies are also easier to form due to the relatively weak interlayer coupling and the soft Re–S covalent bond in ReS₂.⁶⁰ According to DFT calculations, the sulfur vacancies

in ReS₂ create localized mid-gap levels close to the conduction band, which play the role of donors and hence increase the electron concentration at the surface.^{61,62} Accordingly, sulfur vacancies could be the major origin of SEA in ReS₂. Sulfur vacancies behaving like donors in ReS₂ nanostructures and monolayers have been verified.^{63,64} According to the ARPES results, the variation in the electron concentration of the short aging and long aging surfaces could be attributed to the physically adsorbed and chemically adsorbed oxygen/water molecules on the ReS₂ surface respectively. It is inferred that in the beginning, sulfur vacancies were created by the reaction of ambient oxygen/water molecules and the ReS₂ surface. Free electrons are provided by the donor-like surface states induced by the sulfur vacancies, which results in SEA. A similar result was also observed in MoS₂.³¹ It is likely that partial oxygen starts to fill in the sulfur vacancies or form certain defect complexes after the SEA reaches saturation in a long enough exposure time. This is similar to the surface passivation effect that reduces the surface defect density in many semiconductor material systems. Xu *et al.* reported that the O₂ molecule acts as an electron accumulator in the interaction of O₂ and S vacancies in ReS₂.⁶⁵

2.5. SEA evidenced by scanning tunneling microscopy/spectroscopy (STM/STS)

STM/STS measurements were performed to further support the presence of SEA in ReS₂. Fig. 6 illustrates the STM images and STS spectra of *ex situ*-cleaved, aging (air exposure for two months), and pristine (non-fresh) surfaces of a ReS₂ crystal. The *ex situ*-cleaved surface indicates the surface cleaved in ambient air with exposure time <30 min and the “pristine” surface denotes the crystals with original as-grown surface preserved in atmospheric ambience for over 6 months. The conduction band edge (E_C) and the valence band edge (E_V) are obtained from the onsets of the normalized dI/dV curves at positive and negative sample bias respectively in the STS spectra. The zero bias (0 V) denotes the Fermi level position (E_F). Fig. 6d depicts the E_C right on the E_F ($E_C - E_F = 0$ eV), which implies a high electron concentration on the *ex situ*-cleaved surface of ReS₂. The calculated electron concentration is 8.4×10^{18} – 1.8×10^{19} cm⁻³, which is consistent with the ARPES result of the short aging sample because the air exposure times of the two surface conditions are similar (20–30 min).

For the aging surface exposed to air for 2 months (Fig. 6e), the Fermi level shows a slightly red shift ($E_C - E_F = 0.08$ eV) and the electron concentration was reduced to the range of 3.8×10^{17} – 8.2×10^{17} cm⁻³. A similar phenomenon was also observed by ARPES. In addition, over 6 months long-term aging makes the Fermi level shift to an even lower energy position ($E_C - E_F = 0.25$ eV), Fig. 6f. The electron concentration drops to the range of 5.4×10^{14} – 1.2×10^{15} cm⁻³. This result indicates that the electron concentration could be saturated at the level of 10^{14} or 10^{15} cm⁻³ in the ReS₂ surface due to the slow passivation effect induced by air (oxygen or water) molecules. The characteristic of SEA in ReS₂ is different from MoS₂.

The electron concentration increases monotonically and is unable to be passivated by air exposure in MoS₂. The electron concentration (surface states) increases (generates) and then decreases (annihilates) due to the interaction with foreign molecules, which is first observed for TMD layered semiconductors.

The existence of sulfur defects and oxygen adsorption on the ReS₂ surface can be visualized from the STM images. Fig. 6a–c reveal two types of imperfections (dark and bright defects) on the ReS₂ surface. The *ex situ*-cleaved surface has only dark defects (Fig. 6a) and such feature of defects has been reported for TMDs.^{66–68} Plumadore *et al.* have reported that the dark contrasts in the STM image of ReS₂ are due to the S-vacancies and supported by the simulated STM image.⁶⁹ The S-vacancies in ReS₂ can be attributed to the donor levels close to the CBM edge.⁶³ Chalcogen vacancy defects in TMDs^{70,71} are common due to their low vacancy formation energy compared to metal vacancies.⁵⁹ Hence, the dark defects are likely the sulfur monovacancies. These sulfur vacancies act as donor-like surface states and a high carrier concentration was obtained at the *ex situ*-cleaved surface. The surface aging for 2 months in air was free from the dark defects and shows only bright defects (Fig. 6b). Plumadore *et al.* have reported that the bright contrasts in STM image are due to the oxygen adsorbed on the ReS₂ surface and supported by the simulated STM image.⁶⁹ The oxygen adsorbates in ReS₂ function as acceptors.⁶⁵ Therefore, the bright defects are probably the foreign oxygen atoms/molecules that could react with the sulfur vacancies and/or produce acceptor-like surface states and thus reduce the electron concentration for the surface aging for 2 months. It appears that further increasing the aging time (>6 months) makes the surface fully passivated and very few adsorbed oxygen (bright defects) were observed (Fig. 6c). The electron concentration goes down to a saturation level because surface donors (sulfur vacancies) are mostly deactivated (filled).

2.6. Discussion

The surface band bending induced by SEA in ReS₂ is shown schematically in Fig. 7. The donor-like surface states donate electrons to the conduction band and become positively charged, which leads to electron accumulation near the surface and a downward band bending to maintain charge neutrality. The Fermi level overlapping CBM at the near surface represents high electron density at the *ex situ*-cleaved/short aging surface according to the STS/ARPES results.

In addition, though SEA in ReS₂ has been confirmed, the electron concentration at the surface could be time dependent before the surface becomes stable due to the natural passivation. Considering that our nanoflake devices are fabricated without intentionally controlling air exposure time after mechanical exfoliation, the electron concentration could be in the range of 10^{18} to 10^{19} cm⁻³, because the air exposure time of nanoflakes is approximately 1 to 7 days in our fabrication process. The electron concentration levels of nanoflakes can still result in a substantial SEA effect on the electrical conduc-

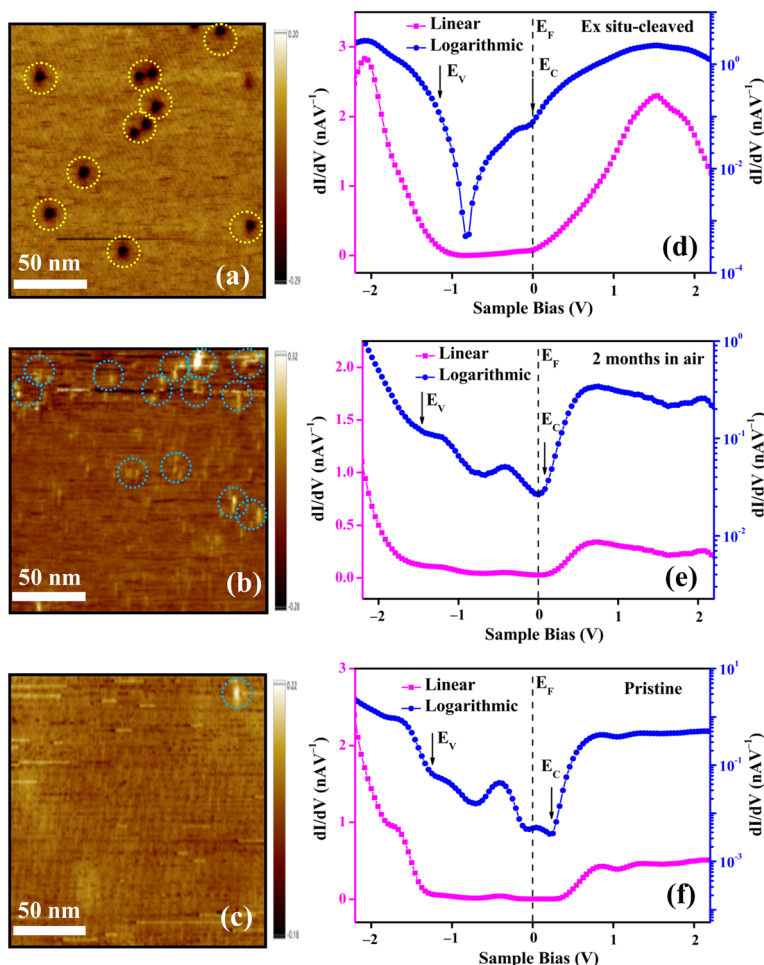


Fig. 6 STM/STS results of different surfaces of the ReS_2 crystal. STM images of (a) *ex situ*-cleaved, (b) aging (2 months in air), and (c) pristine (non-fresh) surfaces of ReS_2 single crystals. The yellow circles denote the dark defects and light blue circles denote the bright defects. The dI/dV curve measurements of (d) *ex situ*-cleaved, (e) aging, and (f) pristine (non-fresh) surfaces of ReS_2 single crystals.

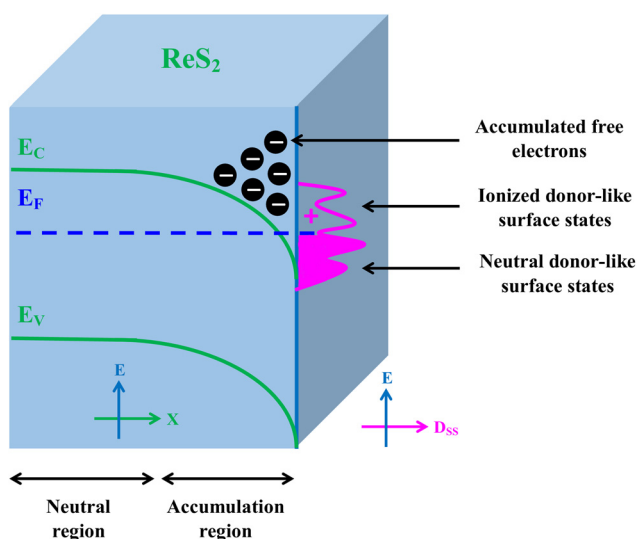


Fig. 7 Schematic of the energy band with surface electron accumulation in ReS_2 . The density of surface states (D_{SS}) versus energy plot is also illustrated.

tivity compared with the values at 10^{15} to 10^{16} cm^{-3} in the inner bulk. This explains why the phenomena of thickness-dependent electrical properties and surface-dominant 2D current transport can still be observed by the conductivity, activation energy, and TLM analyses, as shown in Fig. 4. The finding of SEA also explains the anomalously high carrier concentration ($n = 1.03 \times 10^{18}$ – $8.5 \times 10^{18} \text{ cm}^{-3}$) in ReS_2 nanoflakes and multilayers in the previous reports.^{56,57}

3. Conclusions

We have investigated the in-plane anisotropy in electrical and optoelectronic properties of ReS_2 nanoflakes. Our results revealed that the electrical conductivity parallel to the b -axis ($\parallel b$) is 32 times higher than that perpendicular to the b -axis ($\perp b$). Similarly, optoelectronic anisotropy was also observed, in which the ratio of responsivity $\parallel b$ to $\perp b$ reaches 20. The quasi-2D current flow on the surface in ReS_2 nanoflakes was proposed based on the dimension-dependent electrical pro-

properties. Furthermore, the presence of SEA has been confirmed by ARPES and STS characterization, which supports the surface-dominant electronic transport in ReS₂. Sulfur vacancies which are sensitive to air molecules are suggested to be the major factor resulting in SEA and high conductivity in ReS₂ nanostructures. This work demonstrates a novel understanding of electrical properties of ReS₂ and the potential of polarization-dependent optoelectronic devices using its nanostructures.

4. Experimental

4.1. ReS₂ crystal growth and characterization

The ReS₂ high-quality single crystals are grown with the help of the chemical vapor transport (CVT) technique in the presence of a transporting agent. Rhenium and sulfur powder were purchased from Sigma Aldrich with a high purity of 99.99%. To begin the crystal growth, the powders were first stoichiometrically mixed and loaded in the quartz ampoule with dimensions of 2 cm inner diameter and 30 cm long. Next, iodine was added to the quartz ampoule to transport the vaporized precursors from higher to lower temperature regions. The precursor elements and iodine-loaded quartz ampoules were evacuated to 10⁻⁵ Torr and vacuum-sealed. Following this, the ampoule was placed into a two-zone horizontal furnace. The elemental mix region called the charge zone maintains a temperature of 1080 K, and the empty end of another side of the ampoule is defined as the growth zone kept at 1030 K. The ampoule was maintained in this intermediate condition for two days to allow the precursor to form the ReS₂ compound first. Then the temperature was raised to 1390 K in the charge zone and 1340 K in the growth zone, and maintaining the temperature for seven days to attain high-quality single crystals of ReS₂. Finally, the furnace was cooled down to room temperature with a slow cooling rate of 20 K min⁻¹ to avoid the formation of thermal cracks in the grown single crystals during cooling. The grown single crystals are retrieved from the ampoule growth zone region, and the typical dimensions of the as-grown single crystals were 5 mm × 4 mm × 2 mm in size. The structural properties of CVT grown crystal were characterized by X-ray diffraction (Bruker D2 Phaser) and Raman spectroscopy (Horiba iHR550). The *I-V* measurements of millimeter-sized bulk crystals were performed using silver paste as electrodes.

4.2. ReS₂ nanoflakes device fabrication and characterization

ReS₂ nanoflakes were obtained by a mechanical exfoliation process from CVT grown ReS₂ single crystals with a typical area size of a few square millimeters using a dicing tape. The exfoliated nanoflakes sizes are in a micrometer scale and the thickness varies between a few nanometers to hundred nanometers. For the fabrication of nanoflake devices, the individual nanoflakes were dispersed on the substrate chip of SiO₂ (300 nm)/n⁺-Si with pre-patterned Ti (30 nm)/Au (90 nm) electrodes. The polarized-Raman measurements (Renishaw inVia Raman

microscope system) were carried out in backscattering geometry with a linearly polarized laser of 532 nm. The two platinum (Pt) electrical contacts with a thickness range of 100–500 nm were made on individual ReS₂ nanoflakes using focused-ion beam (FIB-FEI Quanta 3D FEWG) technique. A voltage of 30 kV and a current of 100 pA of ion beam were used for Pt precursor decomposition. The *I-V* measurements of ReS₂ nanoflake devices were performed by a two-probe method. The thicknesses of the nanoflakes were measured using AFM (Bruker Dimension Icon). The temperature dependent conductivity measurements were performed in a ultralow current leakage cryogenic probe station (Lakeshore Cryotronics TTP4). A semiconductor characterization system (Keithley 4200-SCS) was used to source the DC voltage and measure the current.

4.3. ARPES characterization

The ARPES experiment was carried out at the National Synchrotron Radiation Research Center (NSRRC), Hsinchu, Taiwan, using a TLS BL21B1 U9-CGM beamline. The photoemission spectra of ReS₂ single crystals with *in situ*-cleaved (fresh), short aging (20 min exposure in air) and long aging (11 days exposure in air) surfaces were recorded in a UHV chamber (~6.8 × 10⁻¹¹ Torr) equipped with a hemispherical analyzer (Scienta R4000, collecting angle = ±15°). The photon energy of 42 eV was used for all sample spectra at room temperature (RT). The polarization vector is invariably in the angular dispersive plane. The angular and energy resolution are 0.2° and greater than 23 meV respectively. The samples were transferred and measured in the analysis chamber with a base pressure ~6.3 × 10⁻¹¹ Torr after a 1 hour pumping time. The *in situ* fresh surface was cleaved inside the preparation chamber with a base pressure ~1.8 × 10⁻¹⁰ Torr at RT without air exposure and was subsequently measured within 10 minutes exposure in the analysis chamber.

4.4. STM and STS characterization

The STS measurements were carried out by variable temperature scanning tunneling microscopy (VT-STM; Omicron) ultrahigh vacuum chamber with a base pressure of ~6.3 × 10⁻¹¹ Torr. The local density of states (LDOS) of ReS₂ surfaces (*ex situ*-cleaved, air exposure for 2 months, and pristine) was obtained from the *dI/dV* vs. sample bias curves, which are measured using the STS technique. The *ex situ*-cleaved surface was exposed to air less than 30 min before it is loaded into the vacuum chamber. The required pressure in the vacuum chamber was attained in 3 to 4 h and the measurements of all samples were done at room temperature.

Author contributions

Bangolla Hemanth Kumar: methodology, formal analysis, and writing/original draft preparation. Muhammad Yusuf Fakhri: methodology. Ching-Hsuan Lin: methodology. Cheng-Maw Cheng: methodology and investigation. Yi-Hung Lu: methodology. Tsu-Yi Fu: investigation. Pushpa Selvarasu: investi-

gation. Rajesh Kumar: investigation. Raman Sankar: investigation. Ruei-San Chen: conceptualization, supervision, resources, validation, and writing/review & editing. All authors discussed the results and approved the final version of the manuscript.

Conflicts of interest

The authors declare that there are no conflicts to declare.

Acknowledgements

R. S. C. acknowledges the support provided by the Ministry of Science and Technology (MOST) of Taiwan (Grant No. MOST 111-2112-M-011-004-MY3, MOST 108-2628-M-011-001-MY3, MOST 109-2622-E-011-034, and MOST 110-2622-E-011-017). R. S. acknowledges the financial support provided by the Ministry of Science and Technology (MOST) of Taiwan under project numbers NSTC-111-2124-M-001-007, NSTC-110-2112-M-001-065-MY3, and AS iMATE-112-12.

References

- 1 K. Thakar, B. Mukherjee, S. Grover, N. Kaushik, M. Deshmukh and S. Lodha, *ACS Appl. Mater. Interfaces*, 2018, **10**, 36512–36522.
- 2 D. Geng and H. Y. Yang, *Adv. Mater.*, 2018, **30**, 1–23.
- 3 S. Manzeli, D. Ovchinnikov, D. Pasquier, O. V. Yazyev and A. Kis, *Nat. Rev. Mater.*, 2017, **2**, 17033.
- 4 K. F. Mak and J. Shan, *Nat. Photonics*, 2016, **10**, 216–226.
- 5 J. K. Qin, W. Z. Shao, Y. Li, C. Y. Xu, D. D. Ren, X. G. Song and L. Zhen, *RSC Adv.*, 2017, **7**, 24188–24194.
- 6 F. Liu, S. Zheng, A. Chaturvedi, V. Zólyomi, J. Zhou, Q. Fu, C. Zhu, P. Yu, Q. Z. Eng, N. D. Drummond, H. J. Fan, C. Kloc, V. I. Fal'ko, X. He and Z. Liu, *Nanoscale*, 2016, **8**, 5826–5834.
- 7 P. Schiettecatte, D. Poonia, I. Tanghe, S. Maiti, M. Failla, S. Kinge, Z. Hens, L. D. A. Siebbeles and P. Geiregat, *J. Phys. Chem. C*, 2021, **125**, 20993–21002.
- 8 A. Arora, J. Noky, M. Drüppel, B. Jariwala, T. Deilmann, R. Schneider, R. Schmidt, O. DelPozo-Zamudio, T. Stiehm, A. Bhattacharya, P. Krüger, S. Michaelis de Vasconcellos, M. Rohlfing and R. Bratschitsch, *Nano Lett.*, 2017, **17**, 3202–3207.
- 9 R. He, J. A. Yan, Z. Yin, Z. Ye, G. Ye, J. Cheng, J. Li and C. H. Lui, *Nano Lett.*, 2016, **16**, 1404–1409.
- 10 C. An, Z. Xu, W. Shen, R. Zhang, Z. Sun, S. Tang, Y. F. Xiao, D. Zhang, D. Sun, X. Hu, C. Hu, L. Yang and J. Liu, *ACS Nano*, 2019, **13**, 3310–3319.
- 11 F. A. Cevallos, S. Guo, H. Heo, G. Scuri, Y. Zhou, J. Sung, T. Taniguchi, K. Watanabe, P. Kim, H. Park and R. J. Cava, *Cryst. Growth Des.*, 2019, **19**, 5762–5767.
- 12 H. Li, G. Lu, Y. Wang, Z. Yin, C. Cong, Q. He, L. Wang, F. Ding, T. Yu and H. Zhang, *Small*, 2013, **9**, 1974–1981.
- 13 S. Tongay, H. Sahin, C. Ko, A. Luce, W. Fan, K. Liu, J. Zhou, Y. S. Huang, C. H. Ho, J. Yan, D. F. Ogletree, S. Aloni, J. Ji, S. Li, J. Li, F. M. Peeters and J. Wu, *Nat. Commun.*, 2014, **5**, 1–6.
- 14 E. Liu, Y. Fu, Y. Wang, Y. Feng, H. Liu, X. Wan, W. Zhou, B. Wang, L. Shao, C. H. Ho, Y. S. Huang, Z. Cao, L. Wang, A. Li, J. Zeng, F. Song, X. Wang, Y. Shi, H. Yuan, H. Y. Hwang, Y. Cui, F. Miao and D. Xing, *Nat. Commun.*, 2015, **6**, 1–7.
- 15 Y. Xiong, H. W. Chen, D. W. Zhang and P. Zhou, *Phys. Status Solidi RRL*, 2019, **13**, 1–14.
- 16 S. Tongay, J. Zhou, C. Ataca, K. Lo, T. S. Matthews, J. Li, J. C. Grossman and J. Wu, *Nano Lett.*, 2012, **12**, 5576–5580.
- 17 W. Jin, P. C. Yeh, N. Zaki, D. Zhang, J. T. Sadowski, A. Al-Mahboob, A. M. Van DerZande, D. A. Chenet, J. I. Dadap, I. P. Herman, P. Sutter, J. Hone and R. M. Osgood, *Phys. Rev. Lett.*, 2013, **111**, 1–5.
- 18 R. Wang, F. Zhou, L. Lv, S. Zhou, Y. Yu, F. Zhuge, H. Li, L. Gan and T. Zhai, *CCS Chem.*, 2019, **1**, 268–277.
- 19 Y.-C. Lin, H.-P. Komsa, C.-H. Yeh, T. Bjorkman, Z.-Y. Liang, C.-H. Ho, Y.-S. Huang, P.-W. Chiu, A. V. Krashennnikov and K. Suenaga, *ACS Nano*, 2015, 11249–11257.
- 20 D. Li, H. Jussila, L. Karvonen, G. Ye, H. Lipsanen, X. Chen and Z. Sun, *Sci. Rep.*, 2015, **5**, 1–9.
- 21 F. Liu, S. Zheng, X. He, A. Chaturvedi, J. He, W. L. Chow, T. R. Mion, X. Wang, J. Zhou, Q. Fu, H. J. Fan, B. K. Tay, L. Song, R. H. He, C. Kloc, P. M. Ajayan and Z. Liu, *Adv. Funct. Mater.*, 2016, **26**, 1169–1177.
- 22 H. Yuan, X. Liu, F. Afshinmanesh, W. Li, G. Xu, J. Sun, B. Lian, A. G. Curto, G. Ye, Y. Hikita, Z. Shen, S. C. Zhang, X. Chen, M. Brongersma, H. Y. Hwang and Y. Cui, *Nat. Nanotechnol.*, 2015, **10**, 707–713.
- 23 Y. D. Cao, Y. H. Sun, S. F. Shi and R. M. Wang, *Rare Met.*, 2021, **40**, 3357–3374.
- 24 L. R. Bailey, T. D. Veal, C. E. Kendrick, S. M. Durbin and C. F. McConville, *Appl. Phys. Lett.*, 2009, **95**, 1–3.
- 25 T. D. Veal, I. Mahboob, L. F. J. Piper, C. F. McConville, H. Lu and W. J. Schaff, *J. Vac. Sci. Technol., B: Microelectron. Nanometer Struct. – Process., Meas., Phenom.*, 2004, **22**, 2175.
- 26 I. I. Vrubel, D. Yudin and A. A. Pervishko, *Phys. Chem. Chem. Phys.*, 2021, **23**, 4811–4817.
- 27 T. D. Veal, P. H. Jefferson, L. F. J. Piper, C. F. McConville, T. B. Joyce, P. R. Chalker, L. Considine, H. Lu and W. J. Schaff, *Appl. Phys. Lett.*, 2006, **89**, 202110.
- 28 S. K. V. Farahani, T. D. Veal, J. J. Mudd, D. O. Scanlon, G. W. Watson, O. Bierwagen, M. E. White, J. S. Speck and C. F. McConville, *Phys. Rev. B: Condens. Matter Mater. Phys.*, 2014, **90**, 155413.
- 29 P. D. C. King, T. D. Veal, D. J. Payne, A. Bourlange, R. G. Egdell and C. F. McConville, *Phys. Rev. Lett.*, 2008, **101**, 116808.
- 30 K. H. L. Zhang and R. G. Egdell, *Phys. Rev. Lett.*, 2013, **110**, 056803.
- 31 M. D. Siao, W. C. Shen, R. S. Chen, Z. W. Chang, M. C. Shih, Y. P. Chiu and C. M. Cheng, *Nat. Commun.*, 2018, **9**, 1–12.

- 32 Y. S. Chang, C. Y. Chen, C. J. Ho, C. M. Cheng, H. R. Chen, T. Y. Fu, Y. T. Huang, S. W. Ke, H. Y. Du, K. Y. Lee, L. C. Chao, L. C. Chen, K. H. Chen, Y. W. Chu and R. S. Chen, *Nano Energy*, 2021, **84**, 1–13.
- 33 H. Ma, Y. Xing, J. Han, B. Cui, T. Lei, H. Tu, B. Guan, Z. Zeng, B. Zhang and W. Lv, *Adv. Opt. Mater.*, 2022, **10**, 1–7.
- 34 S. Aftab, M. Z. Iqbal, S. Hussain, H. H. Hegazy, F. Kabir, S. H. A. Jaffery and G. Koyyada, *Chem. Eng. J.*, 2023, **469**, 144039.
- 35 A. Venkatesan, H. Ryu, A. Devnath, H. Yoo and S. Lee, *J. Mater. Sci. Technol.*, 2023, **168**, 79–87.
- 36 W. Li, Q. Jia, H. Dong, Z. Wang, Y. Wang, Y. Wu, X. Zhao, Z. Chen and S. Wang, *ACS Appl. Nano Mater.*, 2023, **6**, 512–522.
- 37 J. Yu, Y. Qian, S. Seo, Y. Liu, H. T. D. Bui, N. Q. Tran, J. Lee, A. Kumar, H. Wang, Y. Luo, X. Shao, Y. Cho, X. Liu, M. G. Kim and H. Lee, *J. Energy Chem.*, 2023, **85**, 11–18.
- 38 B. Jariwala, D. Voiry, A. Jindal, B. A. Chalke, R. Bapat, A. Thamizhavel, M. Chhowalla, M. Deshmukh and A. Bhattacharya, *Chem. Mater.*, 2016, **28**, 3352–3359.
- 39 A. Ghetiya, S. H. Chaki, A. J. Khimani, A. B. Hirpara, R. M. Kannaujiya, S. Patel and M. P. Deshpande, *Phys. Status Solidi A*, 2021, **218**, 1–8.
- 40 X. He, F. Liu, P. Hu, W. Fu, X. Wang, Q. Zeng, W. Zhao and Z. Liu, *Small*, 2015, **11**, 5423–5429.
- 41 S. Kim, H. K. Yu, S. Yoon, N. S. Lee and M. H. Kim, *CrystEngComm*, 2017, **19**, 5341–5345.
- 42 D. A. Chenet, O. B. Aslan, P. Y. Huang, C. Fan, A. M. Van DerZande, T. F. Heinz and J. C. Hone, *Nano Lett.*, 2015, **15**, 5667–5672.
- 43 Y. H. Huang, R. S. Chen, J. R. Zhang and Y. S. Huang, *Nanoscale*, 2015, **7**, 18964–18970.
- 44 C. H. Ho, Y. S. Huang and K. K. Tiong, *J. Alloys Compd.*, 2001, **317–318**, 222–226.
- 45 J.-J. Tao, J. Jiang, S.-N. Zhao, Y. Zhang, X.-X. Li, X. Fang, P. Wang, W. Hu, Y. H. Lee, H.-L. Lu and D.-W. Zhang, *ACS Nano*, 2021, **15**, 3241–3250.
- 46 R. S. Chen, W. C. Wang, C. H. Chan, H. P. Hsu, L. C. Tien and Y. J. Chen, *Nanoscale Res. Lett.*, 2013, **8**, 1–8.
- 47 Z. Sun, Z. Liu, J. Li, G. Tai, S. Lau and F. Yan, *Adv. Mater.*, 2012, **24**, 5878–5883.
- 48 S. M. Sze, *Physics of Semiconductor Devices*, John Wiley & Sons, 1981.
- 49 R. S. Chen, C. C. Tang, W. C. Shen and Y. S. Huang, *Nanotechnology*, 2014, **25**, 415706.
- 50 A. Dathbun, Y. Kim, S. Kim, Y. Yoo, M. S. Kang, C. Lee and J. H. Cho, *Nano Lett.*, 2017, **17**, 2999–3005.
- 51 W. S. Leong, Y. Li, K. H. Khoo, S. Y. Quek and J. T. L. Thong, *ACS Nano*, 2015, **9**, 869–877.
- 52 C. M. Corbet, C. McClellan, A. Rai, S. S. Sonde, E. Tutuc and S. K. Banerjee, *ACS Nano*, 2015, **9**, 363–370.
- 53 D. A. Neamen, *Semiconductor physics and devices: Basic Principles*, MC Graw Hill, 2012.
- 54 Z. G. Yu, Y. Cai and Y. W. Zhang, *Sci. Rep.*, 2015, **5**, 1–9.
- 55 D. Ovchinnikov, F. Gargiulo, A. Allain, D. J. Pasquier, D. Dumcenco, C. H. Ho, O. V. Yazyev and A. Kis, *Nat. Commun.*, 2016, **7**, 1–7.
- 56 J. Shim, A. Oh, D. H. Kang, S. Oh, S. K. Jang, J. Jeon, M. H. Jeon, M. Kim, C. Choi, J. Lee, S. Lee, G. Y. Yeom, Y. J. Song and J. H. Park, *Adv. Mater.*, 2016, **28**, 6985–6992.
- 57 N. R. Pradhan, A. McCreary, D. Rhodes, Z. Lu, S. Feng, E. Manousakis, D. Smirnov, R. Namburu, M. Dubey, A. R. H. Walker, H. Terrones, M. Terrones, V. Dobrosavljevic and L. Balicas, *Nano Lett.*, 2015, **15**, 8377–8384.
- 58 K. K. Tiong, C. H. Ho and Y. S. Huang, *Solid State Commun.*, 1999, **111**, 635–640.
- 59 S. Horzum, D. Çakır, J. Suh, S. Tongay, Y. S. Huang, C. H. Ho, J. Wu, H. Sahin and F. M. Peeters, *Phys. Rev. B: Condens. Matter Mater. Phys.*, 2014, **89**, 1–7.
- 60 S. Li, B. Li, X. Feng, L. Chen, Y. Li, L. Huang, X. Fong and K. W. Ang, *npj 2D Mater. Appl.*, 2021, **5**, 1–10.
- 61 J. R. Gadde, A. Karmakar, T. K. Maji, S. Mukherjee, R. Alexander, A. M. R. Sharma, S. Das, A. Mandal, K. Dasgupta, A. Naik, K. Majumdar, R. Hawaldar, K. V. Adarsh, S. K. Ray and D. Karmakar, *Phys. Rev. Mater.*, 2021, **5**, 1–15.
- 62 J. Jiang, C. Ling, T. Xu, W. Wang, X. Niu, A. Zafar, Z. Yan, X. Wang, Y. You, L. Sun, J. Lu, J. Wang and Z. Ni, *Adv. Mater.*, 2018, **30**, 1–6.
- 63 S. Wu, W. Pan, J. Zhang, C. Ma, Y. Shan and L. Liu, *Surf. Interfaces*, 2021, **27**, 101562.
- 64 C. H. Ho and Z. Z. Liu, *Nano Energy*, 2019, **56**, 641–650.
- 65 K. Xu, H. X. Deng, Z. Wang, Y. Huang, F. Wang, S. S. Li, J. W. Luo and J. He, *Nanoscale*, 2015, **7**, 15757–15762.
- 66 N. Sengoku and K. Ogawa, *Jpn. J. Appl. Phys.*, 1995, **34**, 3363–3367.
- 67 X. Liu, I. Balla, H. Bergeron and M. C. Hersam, *J. Phys. Chem. C*, 2016, **120**, 20798–20805.
- 68 R. Addou, L. Colombo and R. M. Wallace, *ACS Appl. Mater. Interfaces*, 2015, **7**, 11921–11929.
- 69 R. Plumadore, M. Baskurt, J. Boddison-Chouinard, G. Lopinski, M. Modarresi, P. Potasz, P. Hawrylak, H. Sahin, F. M. Peeters and A. Luican-Mayer, *Phys. Rev. B*, 2020, **102**, 1–4.
- 70 J. Hong, Z. Hu, M. Probert, K. Li, D. Lv, X. Yang, L. Gu, N. Mao, Q. Feng, L. Xie, J. Zhang, D. Wu, Z. Zhang, C. Jin, W. Ji, X. Zhang, J. Yuan and Z. Zhang, *Nat. Commun.*, 2015, **6**, 1–8.
- 71 S. J. Jung, T. Jeong, J. Shim, S. Park, J. H. Park, B. G. Shin and Y. J. Song, *Curr. Appl. Phys.*, 2019, **19**, 224–229.